Computational Mechanics (2022) 70:945–963
https://doi.org/10.1007/s00466-022-02191-w

ORIGINAL PAPER

Multi-physical modeling and numerical simulation of the thermo-hygro-mechanical treatment of wood

Robert Fleischhauer[1] · **Michael Kaliske**[1]

Received: 7 February 2022 / Accepted: 7 May 2022 / Published online: 2 June 2022

Abstract
The contribution at hand introduces computational modeling and realistic simulation concepts for a comprehensive description of the manufacturing and application of densified wood and wooden structures made from molded densified wood. Wood, as a natural material, is characterized by e.g. a very good mechanical load-bearing capacity related to its density. Nevertheless, the ratio between its mechanical properties and its density can be optimized by densification technology for an expanded use of wood in structural engineering. The wood densification process is not only a mechanical process with large and irreversible deformations, it is also denoted by temperature- and moisture-dependent treatments of the wooden specimens. Thus, the introduced approaches to predict the material and structural characteristics of compressed and molded wood consist of an inelastic and multi-physical constitutive modeling of wood at finite deformations as well as the computation of effective structural properties of wood after the thermo-hygro-mechanical densification process. A successful implementation of the modeling concepts into the finite element method (FEM) is presented, which is verified by numerical investigations. A validation of the numerical results is carried out by use of experimental data at beech wood (*Fagus Sylvatica*, L.), taken from literature.

Keywords Multi-Physical Constitutive Modeling · Finite-Element-Method · Thermo-Hygro-Mechanical Wood Treatment · Structural Investigations in Molded Wooden Tubes

1 Introduction

Wood, as a natural construction material, is characterized by very positive ecological properties, such as its ability to store carbon dioxide (CO_2) over a long time, its renewability as a resource and its easy recyclability. The use of construction materials in industrial applications has a significant influence on the environment and on the climate conditions. The construction industry emits a huge part of all CO_2 contributions, see e.g. [1,30,56]. Wood-based products contribute less to the greenhouse effect than comparable fossil fuel-based products, see [70]. Subsequently, political and social measures, such as focusing on energy and resource efficiency, recycling and reuse, are aiming at the reduction of CO_2 emissions by expanding and optimizing the usage of wooden and wood-based products. Beside its positive ecological properties, wood needs to be economically competitive for its technical features against commonly used construction materials.

Thus, sustainable and optimized wood products are increasingly in the focus of current research by further developing wood processing technologies, see e.g. [44,47,57,65], and for replacing conventional construction materials, see e.g. [50]. Besides the technological developments with respect to wood treatment methods, another research aspect for a deeper engineering is the computational modeling of these technologies by multi-physically constitutive approaches and computational process simulations.

Wood has a complex material structure, whose material properties are depending on the characteristics of the submicroscopic, the microscopic and macroscopic length scale. Macroscopic properties are e.g. the vessel structure, tree ring width as well as heartwood and sapwood, while grain orientation, length of the grains, thickness of the grain walls, proportion of tissue and dimensions of tissue are the characteristic properties at the microscopic length scale. The

✉ Michael Kaliske
michael.kaliske@tu-dresden.de

[1] Institute for Structural Analysis, Technische Universität Dresden, 01062 Dresden, Germany

sub-microscopic properties are the cell walls and the proportion of lignin within the cell walls, see [58].

Due to the natural properties of the annual rings and the grain orientation, wood is considered as an anisotropic material, see e.g. [13,15,18,26,27,36,40,41,45]. Another important property of wooden micro-structures are the ability of binding moisture inside the cell walls and moisture transport through the micro-structure by capillary mechanisms. The mechanical behavior of wood is strongly influenced by its moisture content, see e.g. [63,64,72].

Inelastic effects inside wood, such as viscosity and elasto-plasticity as time-dependent and rate-independent or rate-dependent processes, are focus of the works [39,43,59,60]. Other works model the coupling between the mechanical field and the moisture content, see [7,8,31,35,38,61,62]. The publications [24,25] develop Multi-Fickian approaches in order to capture moisture dependent phenomena in wood. Moisture transport in wood is discussed in detail in [23]. Thermal problems, e.g. drying processes of wood, are addressed in [4,71] among others. Homogenization approaches, motivated by the different length scale dependent structural properties, are developed in e.g. [6,16,17].

The works of [20,21] aim at modeling inelastic hygro-thermo-mechanical phenomena, neglecting the viscosity of wood, in order to capture a wide and general application range.

The contribution at hand successfully introduces a comprehensive and general modeling of densified wood and wooden products. Thus, the only input required into the constitutive formulations of densified wood is the description of undensified wood, since this is also the starting point of the technological production of densified wood.

The paper at hand is structured as follows. Sect. 2 recalls the thermo-hygro-mechanical fundamentals of modeling wood at finite deformations. Sect. 3 deals with the quasi-static hygro-thermo-mechanical finite element and finite surface element formulations. Sect. 4 proposes realistic constitutive descriptions at finite deformations. Sect. 5 introduces the comprehensive modeling of the thermo-hygro-mechanical production process of densified wood and the computation of the densified wood properties. Sect. 6, closes the contribution with a realistic simulation of a compression test on a molded wooden tube made from densified beech wood (*Fagus Sylvatica*). Finally, Sect. 7 briefly summarizes the paper at hand and gives a short outlook to further research quastions and topics.

2 Thermo-hygro-mechanical fundamentals of modeling wood at finite deformations

This section contains the fully coupled partial differential equations, in order to model the thermo-hygro-mechanical behavior of wood. The description of the motion, the temperature change and moisture content as well as the balance principles of multi-physical deformation processes are introduced.

2.1 Solid bodies at different configurations, temperature and moisture content

A solid body B, e.g. a wooden structure or specimen, is considered to be composed of material points $P \in B$, such that these points are connected with a domain $\mathcal{B}$ in $\mathbb{R}^3$. Observing such a material point P while B is moved or moves, introduces to the current position vector $\boldsymbol{x} = \boldsymbol{\chi}(P, t)$. Generally, the configuration $\boldsymbol{\chi}$ is a bijective mapping of $P \in B$ onto $\boldsymbol{x} \in \mathbb{R}^3$. The current configuration $\mathcal{B}_t = \boldsymbol{\chi}_t(B) \subset \mathbb{R}^3$ maps B onto the Euclidean space at a fixed current time t, while at a fixed time t_0, B possesses the reference configuration $\mathcal{B}_0$, with the reference position $\boldsymbol{X} = \boldsymbol{\chi}(P, t_0)$. The mapping $\mathcal{B}_0 = \boldsymbol{\chi}_0(B) \subset \mathbb{R}^3$ is commonly assumed to be a stress-free state with a homogeneous temperature and moisture distribution. The displacement $\boldsymbol{u} := \boldsymbol{x} - \boldsymbol{X}$ is a vector, expressing the difference between the current and the reference position. The derivative

$$\boldsymbol{F} := \mathrm{Grad}\boldsymbol{x} = \frac{\partial \boldsymbol{x}}{\partial \boldsymbol{X}} \tag{1}$$

of the current position vector with respect to the reference position is the deformation gradient $\boldsymbol{F}$. $\boldsymbol{F}$ has a determinant $J = \det \boldsymbol{F}$. The deformation tensor

$$\boldsymbol{C} = \boldsymbol{F}^T \boldsymbol{g} \boldsymbol{F} \tag{2}$$

is the right Cauchy Green deformation tensor. $\boldsymbol{C}$ is the result of the pull-back operation of $\boldsymbol{g}$, the covariant metric tensor of the current configuration, on the reference configuration.

The absolute temperature θ, measured in Kelvin [K], has the property $\theta > 0$. The reference configuration $\mathcal{B}_0$ is homogeneously characterized by an absolute reference temperature θ_0 at t_0. The change of temperature ϑ, e.g. due to an energy input into the observed system, is subsequently computed by $\vartheta := \theta - \theta_0$.

The absolute moisture content ϕ at $\boldsymbol{x} \in \mathcal{B}_t$ is measured as the ratio of the differential mass of bound water and the differential mass of the dry wood e.g. in [kg/kg]. The reference configuration $\mathcal{B}_0$ has a unique distribution of moisture content ϕ_0 within B at t_0 and ϕ_0 is the reference moisture content. The change of moisture content φ, e.g. due to environmental conditions, is subsequently computed by $\varphi := \phi - \phi_0$.

The deformation gradient is multiplicatively split into

$$\boldsymbol{F} = \boldsymbol{F}^E \boldsymbol{F}^P \boldsymbol{F}^\vartheta \boldsymbol{F}^\varphi \,, \tag{3}$$

compare [29,48,49]. This split introduces an elastic part $\boldsymbol{F}^E$, a hygroscopic part $\boldsymbol{F}^\varphi$, a thermal part $\boldsymbol{F}^\vartheta$, and a plastic part $\boldsymbol{F}^P$ of the deformation. Furthermore, taking the natural logarithm of $\boldsymbol{C}$, based on its spectral decomposition, the logarithmic strain measure

$$\boldsymbol{\varepsilon} = \frac{1}{2} \ln \boldsymbol{C} \tag{4}$$

is introduced, see [54]. A subsequent evaluation of Eqs. (2), (3) and (4) enables the introduction of

$$\frac{1}{2} \ln \boldsymbol{C} \approx \boldsymbol{\varepsilon}^E + \boldsymbol{\varepsilon}^P + \boldsymbol{\varepsilon}^\vartheta + \boldsymbol{\varepsilon}^\varphi \, . \tag{5}$$

Due to the evaluation of the logarithm, using the spectral decomposition within the eigenspace of the appropriate quantity, Eq. (5) is not completely an equality, as discussed in detail in [54]. The set of constitutive equations is based on the additive structure of the split

$$\boldsymbol{\varepsilon}^E = \boldsymbol{\varepsilon} - \boldsymbol{\varepsilon}^P - \boldsymbol{\varepsilon}^\vartheta - \boldsymbol{\varepsilon}^\varphi \tag{6}$$

of the total deformation. $\boldsymbol{\varepsilon}^\vartheta$ captures the thermal part of the deformation, and $\boldsymbol{\varepsilon}^\varphi$ is the hygric part of the deformation. $\boldsymbol{\varepsilon}^E$ and $\boldsymbol{\varepsilon}^P$ are the elastic and plastic logarithmic deformations, respectively.

2.2 Mechanical stress measures, thermal and hygroscopic quantities

Considering a traction vector $\boldsymbol{t}$ at $\partial\mathcal{B}_t$ of the current configuration, the Cauchy theorem introduces an infinitesimal surface force $\boldsymbol{t}\mathrm{d}a$ according to

$$\boldsymbol{t}\mathrm{d}a := \boldsymbol{\sigma}\boldsymbol{n}\mathrm{d}a \, , \tag{7}$$

where $\boldsymbol{n}$ is the current outward normal at the point $\boldsymbol{x} \in \partial\mathcal{B}_t$. The Cauchy theorem postulates, that the configuration $\mathcal{B}_t$ may be any subdomain of $\mathcal{B}_t$, thus, $\boldsymbol{\sigma}$ is defined as the true or Cauchy stress tensor for any point $\boldsymbol{x} \in \mathcal{B}_t$.

The transport of thermal energy per time through a point $\boldsymbol{x} \in \partial\mathcal{B}_t$ is given by

$$q_\vartheta \mathrm{d}a = \boldsymbol{q}_\vartheta \cdot \boldsymbol{n}\mathrm{d}a \, , \tag{8}$$

introducing $\boldsymbol{q}_\vartheta$ as the spatial heat flux vector. Similarly, the moisture diffusion at a point $\boldsymbol{x} \in \partial\mathcal{B}_t$ is given by

$$q_\varphi \mathrm{d}a = \boldsymbol{q}_\varphi \cdot \boldsymbol{n}\mathrm{d}a \, , \tag{9}$$

where $\boldsymbol{q}_\varphi$ is the spatial moisture flux vector.

2.3 Hygro-thermo-mechanical equilibrium conditions

The local formulations of the governing evolution equations of a hygro-thermo-mechanical process are given here with respect to the current configuration, see e.g. [20,21,51,52]. This set of equations considers the bound water volume fraction with respect to the mass of a solid wood body B. Thus, the change of density, due to an increase or decrease of moisture content regarding the water, bounded in the cell walls of the wooden microstructure, is captured by

$$\rho = [1 + \phi] \frac{1}{J} \rho_0 \, . \tag{10}$$

Eq. (10) evolves the density of the observed system according to the moisture content at any $\boldsymbol{x} \in \mathcal{B}_t$. Generally, Eq. (10) is only valid below the fiber saturation point of the appropriate wood species.

The first evolution equation (of the unknown displacement field $\boldsymbol{u}$) and equilibrium condition, respectively, is given by Cauchy's equation of motion and describes the equality of the sum of forces acting on B. Its spatial local form reads

$$\boldsymbol{0} = \operatorname{div}(\boldsymbol{\sigma}) \, . \tag{11}$$

Due to the restriction to quasi-static deformation processes, the inertia and body force terms are neglected in Eq. (11). Here, $\boldsymbol{\sigma}$ is the Cauchy stress tensor, compare Eq. (7).

The second evolution equation (of the unknown temperature field ϑ) is given by the transient heat conduction equation. Basis for a consistent derivation of this equation are the balance of energy and the balance of entropy (first and second law of thermodynamics). Both balance laws enable to define a connection of the Helmholtz energy ψ and the Cauchy stress tensor as well as the entropy η according to

$$2\rho\partial_{\boldsymbol{g}}\psi = \boldsymbol{\sigma} \, , \tag{12}$$

$$\eta = -\partial_\theta \psi \, , \tag{13}$$

compare [9,10]. The transient heat conduction equation, neglecting any internal heat source term, reads in its spatial local form

$$\rho c\dot{\theta} = -\operatorname{div}(\boldsymbol{q}_\vartheta) + \underbrace{[\theta\partial_\theta\boldsymbol{\sigma} : \boldsymbol{d}]}_{w_{ext}} - \underbrace{\rho\left[\partial_{\boldsymbol{\mathcal{I}}}\psi - \theta\partial^2_{\boldsymbol{\mathcal{I}}\theta}\psi\right] : \dot{\boldsymbol{\mathcal{I}}}}_{w_{int}} \, . \tag{14}$$

The thermal work done by the Cauchy stresses w_{ext} describes a change of temperature due the change of deformation and, thus, a change of the stress state of the wooden material. The

rate of deformation is captured by the symmetric part of the spatial velocity gradient $\boldsymbol{d} = \mathrm{sym}(\boldsymbol{l})$ with $\boldsymbol{l} = \dot{\boldsymbol{F}}\boldsymbol{F}^{-1}$. The term w_{ext} causes an increase of temperature at compression and cooling at tension at $\boldsymbol{x} \in \mathcal{B}_t$. In contrast, the rate of dissipated energy w_{int} causes heating at $\boldsymbol{x} \in \mathcal{B}_t$ due to any change of the state of the internal variables $\mathcal{I}$. This property is a direct consequence of the strict requirement of a positive local dissipation

$$\mathcal{D}_{loc} := -\partial_{\mathcal{I}}\psi : \dot{\mathcal{I}} \geq 0 \,. \tag{15}$$

The third evolution equation (of the unknown moisture field φ) is given by the modified second Fick's law according to

$$\rho\dot{\phi} = -\mathrm{div}(\boldsymbol{q}_{\varphi}) + \underbrace{\left[-\rho c_{\varphi}\cdot\varphi - \rho c_{\varphi\vartheta}\cdot\vartheta\right]}_{r_{\varphi}(\varphi,\vartheta)} \,. \tag{16}$$

A temperature and moisture dependent source term $r_{\varphi}(\varphi, \vartheta)$ is added to Fick's second law, such that the ability of wood to bind water in its cell walls as well as the interaction of the thermal ϑ and the hygric φ field is described. Eq. (16) is only valid in context of wood below the fiber saturation point.

3 Quasi-static hygro-thermo-mechanical finite element and finite surface element formulations

The system of coupled partial differential equations introduced in Sect. 2.3, is now processed in order to be used for numerical simulations. The computational solution method utilized is the finite element method (FEM). Starting point for deriving the finite element formulations is the Galerkin method and the method of weighted residuals, respectively. The boundary of body B in the current configuration is given by $\partial\mathcal{B}_t$. This boundary is a set of parts of prescribed displacements, temperatures, moisture changes. Additionally, forces, heat flows, moisture absorptive flows can be prescribed on the boundaries of B. The set reads

$$\partial\mathcal{B}_t : \left\{\partial\mathcal{B}_{t_{\boldsymbol{u}}}, \partial\mathcal{B}_{t_{\vartheta}}, \partial\mathcal{B}_{t_{\varphi}}, \partial\mathcal{B}_{t_{\boldsymbol{t}}}, \partial\mathcal{B}_{t_{\boldsymbol{q}^{\vartheta}}}, \partial\mathcal{B}_{t_{\boldsymbol{q}^{\varphi}}}\right\} . \tag{17}$$

The configuration $\mathcal{B}_t$ is subdivided into finite domains $\mathcal{B}_t^E$ reading

$$\mathcal{B}_t = \bigcup_{E=1}^{N} \mathcal{B}_t^E \,. \tag{18}$$

From a methodological point of view, first, the appropriate test functions are introduced according to

$$\delta\boldsymbol{u} := \left\{\delta\boldsymbol{u}(\boldsymbol{x}) \in \mathcal{B}_t \mid \delta\boldsymbol{u} = \boldsymbol{0}\ \forall\, \boldsymbol{x} \in \partial\mathcal{B}_{t_{\boldsymbol{u}}}\right\}, \tag{19}$$

$$\delta\vartheta := \left\{\delta\vartheta(\boldsymbol{x}) \in \mathcal{B}_t \mid \delta\vartheta = 0\ \forall\, \boldsymbol{x} \in \partial\mathcal{B}_{t_{\vartheta}}\right\} , \tag{20}$$

$$\delta\varphi := \left\{\delta\varphi(\boldsymbol{x}) \in \mathcal{B}_t \mid \delta\varphi = 0\ \forall\, \boldsymbol{x} \in \partial\mathcal{B}_{t_{\varphi}}\right\} . \tag{21}$$

Second, the test fields are multiplied to the evolution equation and the product is integrated over the current domain according to

$$\int_{\mathcal{B}_t} \delta\boldsymbol{u}\cdot\mathrm{div}(\boldsymbol{\sigma})\,\mathrm{d}v = 0 \tag{22}$$

for the displacement field. The temperature field equation in its global form reads

$$\int_{\mathcal{B}_t} \delta\vartheta\left(\rho c\dot{\theta} + \mathrm{div}(\boldsymbol{q}_{\vartheta}) - w_{ext} + w_{int}\right)\mathrm{d}v = 0 \,, \tag{23}$$

while the global form for determining the hygroscopic equilibrium reads

$$\int_{\mathcal{B}_t} \delta\varphi\left(\rho\dot{\phi} + \mathrm{div}(\boldsymbol{q}_{\varphi}) - r_{\varphi}\right)\mathrm{d}v = 0 \,. \tag{24}$$

In order to account for the external contributions of the unknown fields, the flux terms in Eqs. (22) to (24) are further processed by rearranging with respect to the differentiation by parts (or the divergence theorems). Thus, Eq. (22) transforms to

$$\int_{\mathcal{B}_t} \boldsymbol{\sigma} : \mathrm{grad}(\delta\boldsymbol{u})\,\mathrm{d}v - \int_{\partial\mathcal{B}_{t_{\boldsymbol{t}}}} \delta\boldsymbol{u}\cdot\boldsymbol{t}\,\mathrm{d}a = 0 \,, \tag{25}$$

and Eq. (23) yields

$$\int_{\mathcal{B}_t} \delta\vartheta\left(\rho c\dot{\theta} - w_{ext} + w_{int}\right)\mathrm{d}v + \int_{\partial\mathcal{B}_{t_{\boldsymbol{q}^{\vartheta}}}} \delta\vartheta\, q_{\vartheta}\,\mathrm{d}a - \int_{\mathcal{B}_t} \mathrm{grad}(\delta\vartheta)\cdot\boldsymbol{q}_{\vartheta}\,\mathrm{d}v = 0 \,. \tag{26}$$

The hygroscopic equilibrium condition reads

$$\int_{\mathcal{B}_t} \delta\varphi\left(\rho\dot{\phi} - r_{\varphi}\right)\mathrm{d}v + \int_{\partial\mathcal{B}_{t_{\boldsymbol{q}^{\varphi}}}} \delta\varphi q_{\varphi}\,\mathrm{d}a - \int_{\mathcal{B}_t} \mathrm{grad}(\delta\varphi)\cdot\boldsymbol{q}_{\varphi}\,\mathrm{d}v = 0 \tag{27}$$

after a further manipulation.

What remains is the discretization of B with isoparametric finite elements according to the isoparametric concept of the FEM, see e.g. [73]. Thus, Lagrange polynomials as functions of the local coordinates $\boldsymbol{\xi}$ are used for the isoparametric shape functions $\boldsymbol{N}(\boldsymbol{\xi})$. Via Jacobi transformation spatial gradients $\boldsymbol{B}(\boldsymbol{\xi})$ are computable, see e.g. [2], as required in Eqs. (25) to (27).

Thus, the set of finite element equations, describing the quasi-static hygro-thermo-mechanical equilibrium read

$$\boldsymbol{R}^I_{\text{mech}_i} = \int\limits_{\mathcal{B}^E_t} \boldsymbol{B}^I_j \boldsymbol{\sigma}_{ij} \,\mathrm{d}v - \int\limits_{\partial\mathcal{B}^E_{t_t}} \boldsymbol{N}^I \boldsymbol{t}_i \,\mathrm{d}a \,, \tag{28}$$

$$\begin{aligned} \boldsymbol{R}^I_{\text{ther}} = &\int\limits_{\mathcal{B}^E_t} \boldsymbol{N}^I \left(\rho c \dot{\theta} - w_{ext} + w_{int}\right) \mathrm{d}v \\ &+ \int\limits_{\partial\mathcal{B}^E_{t_{\boldsymbol{q}^\vartheta}}} \boldsymbol{N}^I q_\vartheta \,\mathrm{d}a - \int\limits_{\mathcal{B}^E_t} \boldsymbol{B}^I_i \boldsymbol{q}_{\vartheta_i} \,\mathrm{d}v \,, \end{aligned} \tag{29}$$

$$\begin{aligned} \boldsymbol{R}^I_{\text{hygr}} = &\int\limits_{\mathcal{B}^E_t} \boldsymbol{N}^I \left(\rho \dot{\phi} - r_\varphi\right) \mathrm{d}v \\ &+ \int\limits_{\partial\mathcal{B}^E_{t_{\boldsymbol{q}^\varphi}}} \boldsymbol{N}^I q_\varphi \,\mathrm{d}a - \int\limits_{\mathcal{B}^E_t} \boldsymbol{B}^I_i \boldsymbol{q}_{\varphi_i} \,\mathrm{d}v \,. \end{aligned} \tag{30}$$

The terms integrated over $\mathcal{B}^E_t$ denote finite elements while the terms integrated over $\partial\mathcal{B}^E_{t_t}$, $\partial\mathcal{B}^E_{t_{\boldsymbol{q}^\vartheta}}$ and $\partial\mathcal{B}^E_{t_{\boldsymbol{q}^\varphi}}$ belong to the finite surface elements.

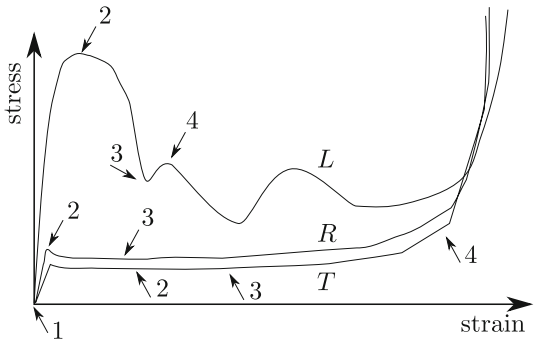

(a) Schematic stress strain curves of three compression tests at Balsa in longitudinal, radial and tangential direction

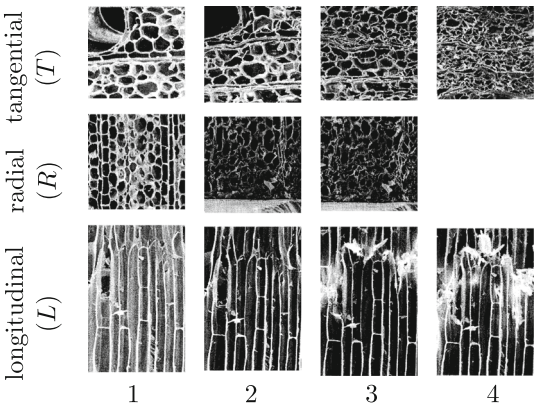

(b) Photos of the microstructure (taken from [15]) of Balsa at the marked deformation situations in Fig. 1a at longitudinal, radial and tangential compression

Fig. 1 The mechanical behavior of Balsa (*Ochroma Pyramidale*) under compression with respect to its longitudinal, radial and tangential grain orientation

4 Constitutive formulations

A comprehensive and general modeling approach to densified wood and wooden products is proposed. Thus, input into the constitutive formulations is the description of undensified wood, since undensified wood is also the starting point of the technological production of densified wood. Having a look at Fig. 1, see also [15,27], where an investigation of Balsa (*Ochroma Pyramidale*) at compressive tests is shown, a clear distinction between the different microstructural behavior of wood with respect to its annual ring orientation and its loading direction is observed. High resistance against deformation is observed, before the collapse of the cell walls, when Balsa is loaded in grain direction and the cell walls deform elastically, see Fig. 1b (L1 to L2). After the first cell wall collapses at the microstructure, a resulting softening at the macrostructural stress strain characteristic is present, see Fig. 1b (L2 and L3). After a consolidation of the state of the cell walls (a non-uniform plateau in the stress strain response) and a stabilization with respect to their fracturing, see Fig. 1b (L3 and L4), Balsa can carry load again and hardening in the high deformation regime is observable. The difference in the loading direction with respect to the grain orientation is changing the mechanical behavior of Balsa drastically. The yield point, i.e.the load value corresponding to the end of the elastic deformations, see Fig. 1a, in radial direction is remarkably lower when compared to the longitudinal direction. After the bending of the cell walls, a densification of the microstructure takes place until it is completely compressed, see Fig. 1b (R2 and R3). After the densification plateau in the stress strain response, hardening, due to the compact microstructure and its ability to carry load, takes place, see Fig. 1a. Similarly, the deformation process in tangential direction is characterized by yielding, densification plateau and hardening at large deformations, see Figs. 1a and 1b.

In the following, the constitutive descriptions, which account for modeling the elastic, the inelastic, the temper-

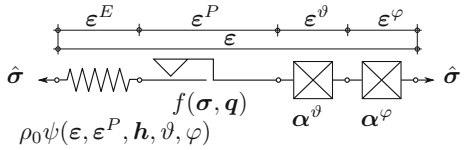

Fig. 2 The rheological interpretation of the constitutive description in the logarithmic strain space

ature and moisture dependent material response of wood at finite deformations, are introduced according to Fig. 2. The constitutive description considers the intrinsic anisotropic elasticity of wood. The longitudinal direction with respect to the grains will be given the subscript L. The perpendicular directions to the grains will be given the subscripts T for tangential and R for the radial direction with respect to the tree trunk axis.

The elastic part of the deformation corresponds to the Helmholtz energy, the inelastic part of the deformation is assumed to be an irreversible deformation, reflecting the state of a damaged microstructure. The phenomenological hardening part of the formulation captures macrostructural hardening observed for all material directions L, R, T. The hygric and thermal expansion is modeled by the corresponding deformation measures in connection with appropriate anisotropic material coefficients.

4.1 Helmholtz energy, Cauchy stresses and hardening response

The Cauchy stresses depend on ρ, the current averaged density, defined in Eq. (10). Furthermore, the link between the Cauchy stresses and the Helmholtz energy $\psi = \psi(\boldsymbol{\varepsilon}, \boldsymbol{\mathcal{I}}, \vartheta, \varphi)$ is given by the logarithmic strain measures, see Sect. 2.1, as well as the logarithmic stress measures $\hat{\boldsymbol{\sigma}}$ related to the current configuration $\mathcal{B}_t$ at time t. The Helmholtz energy serves as a potential for the logarithmic stresses and and the entropy, compare Eq. (13). The set of internal variables $\boldsymbol{\mathcal{I}}$ represents the state of inelasticity of the material at time t and is here defined as $\boldsymbol{\mathcal{I}} : \{\boldsymbol{\varepsilon}^P, \boldsymbol{h}\}$. $\boldsymbol{h}$ is a kinematic hardening strain. Recalling Eq. (4), Eq. (10) and reformulating Eq. (12)

$$\boldsymbol{\sigma} = \frac{\rho}{\rho_0}\frac{\partial \rho_0 \psi}{\partial \boldsymbol{\varepsilon}} : 2\frac{\partial \boldsymbol{\varepsilon}}{\partial \boldsymbol{g}} = \frac{\rho}{\rho_0}\hat{\boldsymbol{\sigma}} : 2\frac{\partial \boldsymbol{\varepsilon}}{\partial \boldsymbol{g}} \tag{31}$$

leads the definition of the logarithmic stress measures $\hat{\boldsymbol{\sigma}}$ and the logarithmic projection tensor $2\partial_{\boldsymbol{g}}\boldsymbol{\varepsilon}$. The latter one can be computed via the spectral representation of $\boldsymbol{C}$, see [54].

The works [15,27] analyze the mechanical behavior of balsa wood. The same and similar behavior can be observed at compression applied to other species of hardwood and softwood, e.g. spruce wood (*Picea Abies*), beech wood (*Fagus Sylvatica*) or oak wood (*Quercus Robur*), see [34,56]. Even compression at high temperature shows a similar stress strain characteristic. Thus, a generalized Helmholtz energy, capturing different stages of the stress and deformation dependency over a certain range of temperatures and moisture contents, is proposed. The energy is stored in a multiphysical and anisotropic spring according to

$$\begin{aligned}\rho_0\psi(\boldsymbol{\varepsilon}, \boldsymbol{\varepsilon}^P, \boldsymbol{h}, \vartheta, \varphi) =& W_{htm}(\boldsymbol{\varepsilon}^E) \\ &+ W_t(\vartheta) + W_q(\boldsymbol{h}) \,,\end{aligned} \tag{32}$$

where W_{htm} denotes the hygro-thermo-mechanical part, W_t captures the purely thermal characteristics and W_q is the latent part of the energy stored in the system at $\boldsymbol{x} \in \mathcal{B}_t$. The specific and invariant based form of W_{htm} reads

$$\begin{aligned}W_{htm} =& \frac{\lambda_{TR}}{2}(\mathrm{tr}\boldsymbol{\varepsilon}^E)^2 + \mu_{TR}\boldsymbol{\varepsilon}^E : \boldsymbol{\varepsilon}^E \\ &+ \frac{\lambda_L}{2}I_{4_L}^2 + \frac{\lambda_{TR}}{2}\cdot\left(\beta_{TR}^{\lambda}\cdot I_{4_T}^2 + I_{4_R}^2\right) \\ &\mu_L I_{5_L} + \mu_{TR}\left(\beta_{TR}^{\mu}\cdot I_{5_T} + I_{5_R}\right) \,,\end{aligned} \tag{33}$$

compare [11,42], while W_t is assumed to be characterized by

$$\begin{aligned}W_t(\vartheta) =& -\rho_0 c\left(-\vartheta + \theta\ln\left(\frac{\theta}{\theta_0}\right)\right) \\ &- \frac{\vartheta^2}{2}\cdot\frac{\partial^2 W_{htm}}{\partial\vartheta\,\partial\vartheta} \,.\end{aligned} \tag{34}$$

Eq. (33) governs an underlying isotropic effect, that is superimposed by the anisotropy with respect the appropriate invariants, which are computed according to

$$I_{4_L} = I_{4_L}(\boldsymbol{\varepsilon}^E) := \boldsymbol{L} : (\boldsymbol{\varepsilon}^E\boldsymbol{L}) \,, \tag{35}$$
$$I_{4_R} = I_{4_R}(\boldsymbol{\varepsilon}^E) := \boldsymbol{R} : (\boldsymbol{\varepsilon}^E\boldsymbol{R}) \,, \tag{36}$$
$$I_{4_T} = I_{4_T}(\boldsymbol{\varepsilon}^E) := \boldsymbol{T} : (\boldsymbol{\varepsilon}^E\boldsymbol{T}) \,, \tag{37}$$
$$I_{5_L} = I_{5_L}(\boldsymbol{\varepsilon}^E) := \boldsymbol{L} : (\boldsymbol{\varepsilon}^E\boldsymbol{\varepsilon}^E\boldsymbol{L}) \,, \tag{38}$$
$$I_{5_R} = I_{5_R}(\boldsymbol{\varepsilon}^E) := \boldsymbol{R} : (\boldsymbol{\varepsilon}^E\boldsymbol{\varepsilon}^E\boldsymbol{R}) \,, \tag{39}$$
$$I_{5_T} = I_{5_T}(\boldsymbol{\varepsilon}^E) := \boldsymbol{T} : (\boldsymbol{\varepsilon}^E\boldsymbol{\varepsilon}^E\boldsymbol{T}) \,. \tag{40}$$

The material directions are given by three vectors at $\boldsymbol{x} \in \mathcal{B}_t$, where $\boldsymbol{L}$ denotes the vector pointing in longitudinal direction, $\boldsymbol{R}$ indicated radial and $\boldsymbol{T}$ tangential direction with respect to the tree trunk axis. In contrast to most of the works that contain modeling approaches of wood, the contribution at hand makes use of the Lamé parameters instead of Young's moduli and Poisson's ratios, compare [28,32,37,68], which is in accordance with the finite deformation assumptions and the underlying kinematics.

The logarithmic stresses take the form

$$\hat{\boldsymbol{\sigma}}_{ij} = \lambda_{TR}\mathrm{tr}\boldsymbol{\varepsilon}^E\delta_{ij} + 2\mu_{TR}\boldsymbol{\varepsilon}_{ij}^E$$

$$
\begin{aligned}
&+ \lambda_L I_{4_L} \frac{1}{2} \left(\boldsymbol{L}_i \boldsymbol{L}_j + \boldsymbol{L}_j \boldsymbol{L}_i \right) \\
&+ \lambda_{TR} \beta_{TR}^{\lambda} I_{4_T} \frac{1}{2} \left(\boldsymbol{T}_i \boldsymbol{T}_j + \boldsymbol{T}_j \boldsymbol{T}_i \right) \\
&+ \lambda_{TR} I_{4_R} \frac{1}{2} \left(\boldsymbol{R}_i \boldsymbol{R}_j + \boldsymbol{R}_j \boldsymbol{R}_i \right) \\
&+ \mu_L \left(\boldsymbol{L}_i \boldsymbol{\varepsilon}_{jk}^E \boldsymbol{L}_k + \boldsymbol{L}_j \boldsymbol{\varepsilon}_{ik}^E \boldsymbol{L}_k \right) \\
&+ \mu_{TR} \beta_{TR}^{\mu} \left(\boldsymbol{T}_i \boldsymbol{\varepsilon}_{jk}^E \boldsymbol{T}_k + \boldsymbol{T}_j \boldsymbol{\varepsilon}_{ik}^E \boldsymbol{T}_k \right) \\
&+ \mu_{TR} \left(\boldsymbol{R}_i \boldsymbol{\varepsilon}_{jk}^E \boldsymbol{R}_k + \boldsymbol{R}_j \boldsymbol{\varepsilon}_{ik}^E \boldsymbol{R}_k \right) , \qquad (41)
\end{aligned}
$$

after application of the derivative in Eq. (31). For modeling the destruction, densification and compaction of the microstructure of wood, see e.g. Fig. 1, a rate-independent, multi-surface yielding and an anisotropic hardening plasticity formulation are proposed. Thus, a hardening strain-like tensor $\boldsymbol{h}$ is introduced. The conjugate symmetric hardening stress tensor $\boldsymbol{q}$ can be derived from the anisotropic hardening potential $W_q(\boldsymbol{h})$ according to

$$
\begin{aligned}
\boldsymbol{q}_{ij} &:= - \frac{\partial W_q(\boldsymbol{h})}{\partial \boldsymbol{h}_{ij}} \\
&= -k_{1_L}^h \left(\boldsymbol{L}_i \boldsymbol{h}_{jk} \boldsymbol{L}_k + \boldsymbol{L}_j \boldsymbol{h}_{ik} \boldsymbol{L}_k \right) \\
&- k_{TR}^h \left(\boldsymbol{T}_i \boldsymbol{h}_{jk} \boldsymbol{T}_k + \boldsymbol{T}_j \boldsymbol{h}_{ik} \boldsymbol{T}_k \right. \\
&\left. + \boldsymbol{R}_i \boldsymbol{h}_{jk} \boldsymbol{R}_k + \boldsymbol{R}_j \boldsymbol{h}_{ik} \boldsymbol{R}_k \right) \\
&- k_{2_L}^h \left(I_{4_L}^h \right)^2 \left(\boldsymbol{L}_i \boldsymbol{L}_j + \boldsymbol{L}_j \boldsymbol{L}_i \right) . \qquad (42)
\end{aligned}
$$

Eq. (42) denotes a phenomenological approach to describe the changes and rearrangements of the microstructure of wood, especially at finite deformations. The next step towards a complete set of constitutive equations is the formulation of the evolution equations of the internal variables according to the material behavior of wood. Thus, they are given by

$$
\dot{\boldsymbol{\varepsilon}}^P = \sum_{\alpha=1}^{12} \dot{\gamma}_\alpha \partial_{\hat{\boldsymbol{\sigma}}} f_\alpha(\hat{\boldsymbol{\sigma}}, \boldsymbol{q}) , \qquad (43)
$$

$$
\dot{\boldsymbol{h}} = \sum_{\alpha=1}^{12} \dot{\gamma}_\alpha \partial_{\boldsymbol{q}} f_\alpha(\hat{\boldsymbol{\sigma}}, \boldsymbol{q}) , \qquad (44)
$$

where the index $\square_\alpha$ denotes the yield surface $f_\alpha(\hat{\boldsymbol{\sigma}}, \boldsymbol{q})$. These yield surfaces characterize different yield levels at different material directions with respect to the grain orientation. Wood shows different yield levels, when loaded differently with respect to its tree trunk axis, see e.g. Fig. 1. Eq. (43) is an associated plastic flow rule and Eq. (44) is the hardening law, compare [67]. Both evolution equations follow the thermodynamic restrictions of a positive dissipation, whenever $\left\| \boldsymbol{\varepsilon}^P \right\| \neq 0 \wedge \|\boldsymbol{h}\| \neq 0$. The inelastic consistency parameters $\dot{\gamma}_\alpha$ in Eq. (43) and Eq. (44) follow the Kuhn-Tucker complementary conditions

$$
\dot{\gamma}_\alpha \geq 0 , \qquad (45)
$$

$$
f_\alpha(\hat{\boldsymbol{\sigma}}, \boldsymbol{q}) \leq 0 , \qquad (46)
$$

$$
\dot{\gamma}_\alpha f_\alpha(\hat{\boldsymbol{\sigma}}, \boldsymbol{q}) = \dot{\gamma}_\alpha \dot{f}_\alpha(\hat{\boldsymbol{\sigma}}, \boldsymbol{q}) \equiv 0 . \qquad (47)
$$

The active yield surfaces of Eqs. (48) to (59) are determined according to Eq. (46). Active means that every $f_\alpha > 0$ is denoting a non-admissible logarithmic stress state outside of the elastic domain $\mathbb{E} := \{(\hat{\boldsymbol{\sigma}}, \boldsymbol{q}) \in \mathbb{R}^6 \times \mathbb{R}^6 \mid f_\alpha < 0 \, \forall \, \alpha\}$. Generally, geometric interpretations of admissible and non-admissible logarithmic stress states in the logarithmic stress space are similar to the interpretations depicted in [14,67]. Eq. (31), Eq. (4) and Eq. (5) as well as the evolution equations Eq. (43) and Eq. (44) define a set of non-linear coupled partial differential equations in time. Regardless of the actual state of deformation, as outlined in [54], the chosen kinematic approach, see Sect. 2.1, preserves a solution strategy similar to small strain theory as depicted e.g. in [66]. The yield surfaces are described with respect to the logarithmic stress components according to

$$
f_1 := -\hat{\boldsymbol{\sigma}}_{11} - \left(\boldsymbol{\sigma}_{c_{11}}^Y - \boldsymbol{q}_{11} \right) , \qquad (48)
$$

$$
f_2 := -\hat{\boldsymbol{\sigma}}_{22} - \left(\boldsymbol{\sigma}_{c_{22}}^Y - \boldsymbol{q}_{22} \right) , \qquad (49)
$$

$$
f_3 := -\hat{\boldsymbol{\sigma}}_{33} - \left(\boldsymbol{\sigma}_{c_{33}}^Y - \boldsymbol{q}_{33} \right) , \qquad (50)
$$

$$
f_4 := -\hat{\boldsymbol{\sigma}}_{12} - \left(\boldsymbol{\sigma}_{c_{12}}^Y - \boldsymbol{q}_{12} \right) , \qquad (51)
$$

$$
f_5 := -\hat{\boldsymbol{\sigma}}_{13} - \left(\boldsymbol{\sigma}_{c_{13}}^Y - \boldsymbol{q}_{13} \right) , \qquad (52)
$$

$$
f_6 := -\hat{\boldsymbol{\sigma}}_{23} - \left(\boldsymbol{\sigma}_{c_{23}}^Y - \boldsymbol{q}_{21} \right) , \qquad (53)
$$

for the negative stresses and

$$
f_7 := \hat{\boldsymbol{\sigma}}_{11} - \boldsymbol{\sigma}_{t_{11}}^Y , \qquad (54)
$$

$$
f_8 := \hat{\boldsymbol{\sigma}}_{22} - \boldsymbol{\sigma}_{t_{22}}^Y , \qquad (55)
$$

$$
f_9 := \hat{\boldsymbol{\sigma}}_{33} - \boldsymbol{\sigma}_{t_{33}}^Y , \qquad (56)
$$

$$
f_{10} := \hat{\boldsymbol{\sigma}}_{12} - \boldsymbol{\sigma}_{t_{12}}^Y , \qquad (57)
$$

$$
f_{11} := \hat{\boldsymbol{\sigma}}_{13} - \boldsymbol{\sigma}_{t_{13}}^Y , \qquad (58)
$$

$$
f_{12} := \hat{\boldsymbol{\sigma}}_{23} - \boldsymbol{\sigma}_{t_{23}}^Y , \qquad (59)
$$

in case of positive stresses, where the symmetry of $\hat{\boldsymbol{\sigma}}$ is considered. The set of equations, Eqs. (48) to (59) defines the elastic domain $\mathbb{E}$ within the logarithmic stress space. The hardening stresses $\boldsymbol{q}$ are not entering the tensile yield surfaces, since brittle failure at the yield stress is assumed. Thus, post-yield hardening behavior at tension is not governed by Eq. (54) to Eq. (59). The composition of $\boldsymbol{\sigma}_c^Y$ according to

$$\begin{aligned}\boldsymbol{\sigma}^{Y}_{c_{ij}} := &\|\boldsymbol{L}_i\boldsymbol{L}_j\|\sigma^{Y}_{c_L}\\ &+\|\boldsymbol{R}_i\boldsymbol{R}_j\|\sigma^{Y}_{c_R}\\ &+\|\boldsymbol{T}_i\boldsymbol{T}_j\|\sigma^{Y}_{c_T}\\ &+0.5\cdot\|\boldsymbol{L}_i\boldsymbol{R}_j+\boldsymbol{L}_j\boldsymbol{R}_i\|\sigma^{Y}_{c_{LR}}\\ &+0.5\cdot\|\boldsymbol{T}_i\boldsymbol{R}_j+\boldsymbol{T}_j\boldsymbol{R}_i\|\sigma^{Y}_{c_{TR}}\\ &+0.5\cdot\|\boldsymbol{L}_i\boldsymbol{T}_j+\boldsymbol{L}_j\boldsymbol{T}_i\|\sigma^{Y}_{c_{LT}}\end{aligned} \tag{60}$$

and $\boldsymbol{\sigma}^{Y}_{t}$ according to

$$\begin{aligned}\boldsymbol{\sigma}^{Y}_{t_{ij}} := &\|\boldsymbol{L}_i\boldsymbol{L}_j\|\sigma^{Y}_{t_L}\\ &+\|\boldsymbol{R}_i\boldsymbol{R}_j\|\sigma^{Y}_{t_R}\\ &+\|\boldsymbol{T}_i\boldsymbol{T}_j\|\sigma^{Y}_{t_T}\\ &+0.5\cdot\|\boldsymbol{L}_i\boldsymbol{R}_j+\boldsymbol{L}_j\boldsymbol{R}_i\|\sigma^{Y}_{t_{LR}}\\ &+0.5\cdot\|\boldsymbol{T}_i\boldsymbol{R}_j+\boldsymbol{T}_j\boldsymbol{R}_i\|\sigma^{Y}_{t_{TR}}\\ &+0.5\cdot\|\boldsymbol{L}_i\boldsymbol{T}_j+\boldsymbol{L}_j\boldsymbol{T}_i\|\sigma^{Y}_{t_{LT}}\end{aligned} \tag{61}$$

are proposed and provide the means to account for the yield stress in grain direction and perpendicular to it.

4.2 Temperature and moisture dependency

The logarithmic thermal deformations $\boldsymbol{\varepsilon}^{\vartheta}$ are constitutively described by

$$\boldsymbol{\varepsilon}^{\vartheta} = \boldsymbol{\alpha}^{\vartheta}\vartheta\ , \tag{62}$$

where

$$\boldsymbol{\alpha}^{\vartheta}_{ij} := \boldsymbol{L}_i\boldsymbol{L}_j\alpha^{L}_{t} + \boldsymbol{R}_i\boldsymbol{R}_j\alpha^{R}_{t} + \boldsymbol{T}_i\boldsymbol{T}_j\alpha^{T}_{t} \tag{63}$$

introduces the anisotropic thermal expansion coefficients $\boldsymbol{\alpha}^{\vartheta}_{ij}$ for the accompanying coordinate direction. The logarithmic moisture dependent deformations $\boldsymbol{\varepsilon}^{\varphi}$ are introduced according to

$$\boldsymbol{\varepsilon}^{\varphi} = \boldsymbol{\alpha}^{\varphi}\varphi\ , \tag{64}$$

where

$$\boldsymbol{\alpha}^{\varphi}_{ij} := \boldsymbol{L}_i\boldsymbol{L}_j\alpha^{L}_{m} + \boldsymbol{R}_i\boldsymbol{R}_j\alpha^{R}_{m} + \boldsymbol{T}_i\boldsymbol{T}_j\alpha^{T}_{m} \tag{65}$$

contain the swelling and shrinking numbers of wood.

The spatial heat flux vector in Eq. (8) is described by an adaption of Fourier's law for isotropic materials with respect to anisotropy and density dependency, according to

$$\boldsymbol{q}_{\vartheta} = -\frac{\rho}{\rho_0}\boldsymbol{K} : \mathrm{grad}(\vartheta)\ . \tag{66}$$

The thermal conductivity coefficients $k^{I} > 0 \mid I = T, R, L$ are proposed to enter $\boldsymbol{K}$ by

$$\boldsymbol{K}_{ij} := \boldsymbol{L}_i\boldsymbol{L}_j k^{L} + \boldsymbol{R}_i\boldsymbol{R}_j k^{R} + \boldsymbol{T}_i\boldsymbol{T}_j k^{T} \tag{67}$$

and describe the ability of wood to transport thermal energy per time in the appropriate global coordinate directions, having units of e.g. [energy/(length time temperature)]. This transport process is density dependent, although $\boldsymbol{K}_{ij}$ are constant with respect to density.

Similarly, the spatial moisture diffusion vector in Eq. (9) is specified as

$$\boldsymbol{q}_{\varphi} = -\frac{\rho}{\rho_0}\boldsymbol{D} : \mathrm{grad}(\varphi)\ , \tag{68}$$

where

$$\boldsymbol{D}_{ij} := \boldsymbol{L}_i\boldsymbol{L}_j d^{L} + \boldsymbol{R}_i\boldsymbol{R}_j d^{R} + \boldsymbol{T}_i\boldsymbol{T}_j d^{T} \tag{69}$$

contains the moisture diffusion coefficients $d^{I} > 0 \mid I = T, R, L$ in global coordinate directions. These coefficients are measured in e.g. [mass/(length time)] and describe therefore the ability of transporting a certain mass of moisture per time and the appropriate coordinate direction. This description is based on Fick's first law and is only valid below the wood specific fiber saturation point.

Subsequently, the thermal energy transport per time through a point at the surface $\partial\mathcal{B}_{t_{\boldsymbol{q}^{\vartheta}}}$ is constitutively described according to the requirement of Eq. (26) if $\partial\mathcal{B}_{t_{\boldsymbol{q}^{\vartheta}}}$ is present. The specific formulation reads

$$q_{\vartheta} = h_{\vartheta}\,(\theta - \theta_{\infty}) \tag{70}$$

and is valid for any absolute temperature $\theta > 0$ and contains $\theta_{\infty} > 0$ as the surrounding temperature of the environment. Eq. (70) is based on Newton's law of cooling, compare [12,46] among others and contains h_{ϑ} measured in e.g. [energy/(time area temperature)].

The amount of moisture, that diffuses either out of the wood or into the wood at $\partial\mathcal{B}_{t_{\boldsymbol{q}^{\varphi}}}$, compare Eq. (27), is constitutively modeled by

$$q_{\varphi} = h_{\varphi}\,(\phi - \phi_{\infty})\cdot\left(1 - \frac{\phi}{\phi_{FSP}}\right)\ . \tag{71}$$

Eq. (71) contains h_{φ} as the surface diffusion coefficient, measured in e.g. [mass/(time area)], which expresses the ability of the wooden surfaces to diffuse a certain amount of water per time in/out of their area. Furthermore, Eq. (71) is modeled such that it considers the fiber saturation point, i.e. whenever the absolute amount of bound water $\phi = \phi_0 + \varphi$ reaches the fiber saturation point ϕ_{FSP}, no diffusive effects will take place anymore at the surface.

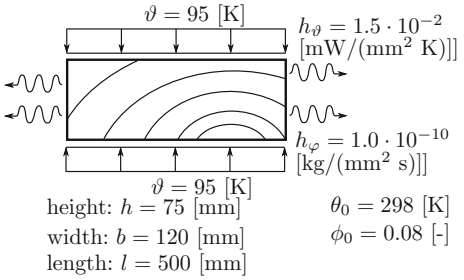

Fig. 3 Heating for 30 minutes as pre-conditioning prior to densification

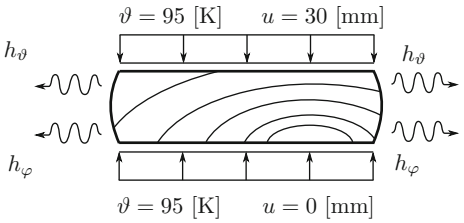

Fig. 4 40 % radial densification at a loading speed of $\dot{u} = 2$ [mm/min]

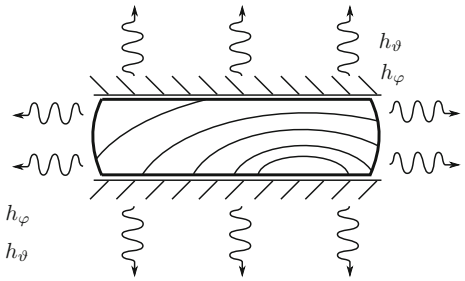

Fig. 5 Holding and post-conditioning after densification

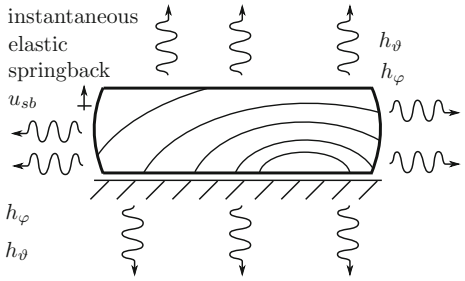

Fig. 6 Observable instantaneous springback (u_{sb}) after removing the top surface holding condition

Both modeling approaches of Eqs. (66) and (68) are explicitly depending on the density, i.e. a change of the current density will influence both transport mechanisms.

5 Comprehensive modeling of the thermo-hygro-mechanical production process of densified wood and the computation of the densified wood properties

The following section introduces an comprehensive approach of the production process of densified wood under consideration of its thermo-hygro-mechanical properties. Furthermore, a direct prediction method of the densified wood properties is proposed and its applicability to the densification of beech wood is demonstrated. One advantage of a direct computation of the densified wood properties is the omission of a parameter identification process at densified wooden structures.

5.1 Modeling the densification process

A description of the geometry, boundary conditions, annual ring orientation and loading for the production of a densified beech wood (*Fagus Sylvatica*) board for the environmental conditions of $\theta_\infty = 25$ [°C] and $\phi_\infty = 0.08$ [-] is given in Figs. 3 to 6. The specific choice of the production process parameters, such as combination of temperature, densification ratio and direction, is made in order to resemble the manufacturing of the compressed beech wood specimens in [56]. The proposed comprehensive modeling approach is not restricted to a specific set of production parameters. Chemical transformations of wood cells are not captured by the governing equations in Sects. 2, 3 and 4. The modeling approach is based on the assumption that wood remains wood, even after a modification by different multi-physical technologies. This means, the thermo-hygro-mechanical material parameters of undensified wood can change their values but remain valid for the description of densified wood. Thus, the proposed method can capture any change of material properties, regardless if the reason for the change is induced by a change of moisture content, temperature or state of densification of the wood at the engineering length scale.

The production of the densified beech wood board, as explained in detail in e.g. [34] and compare [57], starts by heating of the undensified board. Depending on the size and pressure capabilities of the mechanical densification device, the geometry of the board has to be chosen. Here, a relatively small geometry of the board is assumed, such that a standard compression machine can be considered to realize a radial densification of up to 40%. The heating is assumed to be carried out by the steel plates of the compression machine. As depicted in Fig. 3, 30 minutes of pre-heating via top and bottom surfaces of the board is assumed. Following the heating, the densification takes place. Therefore, the top steel plate, having a temperature of approx. 120 [°C], is displaced in compression direction at a speed of 2 [mm/min] until 40 % of the initial height remains for the specimen, see Fig. 4. The specific choice of 120 [°C] follows the data published in [56]. No chemical transformation of the beech wood close to the

heating plates of the hot press is assumed. Only compression of the earlywood cells is considered due to the densification in radial direction. The next step is cooling down of the specimen. Therefore, temperature boundary conditions are removed and the steel plates are fixed with respect to movement and stay at the required densification level, see Fig. 5. After the holding time, the top steel plate is removed and an instantaneous springback is observed, i.e. the top surface of the board moves against its compression direction, until an equilibrium with the internal stress state and the environmental conditions is achieved, see Fig. 6. The springback, here denoted as u_{sb}, depends on the cooling and holding time, see also [56]. The longer the holding conditions are applied, the less amount of springback deformation occurs.

5.2 Direct computation of densified wood properties

First, the volume averaging of appropriate quantities with respect to the current configuration is defined by

$$\overline{\square} := \frac{1}{v}\int_{\mathcal{B}_t} \square \mathrm{d}v \,, \tag{72}$$

according to the geometric mean value computation, see e.g. [3,19,22,53,69]. This step is required in order to determine the material properties of densified wood as a result of the densification process described in Figs. 3 to 6. The novelty of the proposed approach is the computation of the mean or effective Helmholtz energy ($\overline{\rho\psi}_{htm}$) stored in the whole structure. Therefore, in a first step,

$$\rho\psi_{htm} = \frac{\rho}{\rho_0}\rho_0\psi_{htm} = \frac{\rho}{\rho_0}W_{htm} \tag{73}$$

is computed at each integration point, compare Eq. (33). Next, the energy related to the current density is weighted by the infinitesimal volume dv and, finally, the energy integral of all integration points is divided by the current volume v, according to

$$\overline{\rho\psi}_{htm}(P_0) = \frac{1}{v}\int_{\mathcal{B}_t} \rho\psi_{htm}(P_0)\mathrm{d}v \,. \tag{74}$$

Thus, $\overline{\rho\psi}_{htm}$, representing the structural average of the energy induced by loading and boundary conditions as well as annual ring orientation, is computed as a function of the initial parameters $P_0 := \{\lambda_L, \lambda_{TR}, \mu_L, \mu_{TR}, \beta^{\lambda}_{TR}, \beta^{\mu}_{TR}\}$. In a next step, $\overline{\rho\psi}_{htm}(P_0)$ at ρ is assumed to be equal to an effective material description $\overline{W}_{htm}$ at $\overline{\rho}_0 = \rho$ with effective parameters ($\overline{P}$) of densified wood, such that

$$\overline{\rho\psi}_{htm}(P_0) = \overline{W}_{htm}(\overline{P}) \tag{75}$$

and is constitutively formulated in the same manner as Eq. (33). Consequently, the key assumption is the equality of the Helmholtz free energy formulation of densified and undensified wood, only differences are related to the densities and the material parameter values. From Eq. (75), a residual for the densified wood state at known ρ, but unknown $\overline{P}$, is computed by

$$\mathcal{R} = \left(\overline{W}_{htm}(\overline{P}) - \overline{\rho\psi}_{htm}(P_0)\right)^2 \,. \tag{76}$$

Eq. (76) is a "least squares error formulation", which now can be solved by standard approaches, such as the Newton method, reading

$$\boldsymbol{0} = \frac{\partial\mathcal{R}}{\partial\overline{P}} + \frac{\partial^2\mathcal{R}}{\partial\overline{P}\partial\overline{P}} : \Delta\overline{P} \tag{77}$$

as a linearization around the root of $\mathcal{R}$. The solution of Eq. (76) is achieved, whenever the iterative update $\overline{P}_{k+1} = \overline{P}_k + \Delta\overline{P}$ vanishes. The final update contains the final set of current material parameters for the densified state of the wooden structure.

5.3 Numerical results

In order to demonstrate the applicability and realistic features of the model and methods proposed, this section shows numerical results. All FEM simulations are carried by the finite element and finite surface elements proposed in Sect. 3, based on the fundamentals in Sect. 2. At first, the initial parameter set of undensified beech wood, listed in Table 1, as identified in [20,21], is applied to model the densification process as described in Figs. 3 to 6. These model parameters for undensified beech wood are valid for a reference temperature of $\theta_0 = 25°\mathrm{C}$, a reference density of $\rho_0 = 6.9\text{E-}07$ kg/mm^3 and a reference moisture content of $\phi_0 = 0.08$. The model parameters are not explicitly a function of temperature or moisture content, since the model itself explicitly considers the multi-physics with respect to a change of density, temperature and moisture content. The finite element mesh, depicted in Fig. 9, is applied to the densification simulation as described above. The size of the finite elements is chosen to be sufficient with respect to the accuracy of the prediction of the numerical results in contrast to the intrinsic uncertainty of the underlying physical problem. A finer resolution of the mesh will not significantly improve the agreement of a single simulation to an average of a huge number of physical experiments.

Table 1 Model parameter set P_0 for undensified beech wood at $\theta_0 = 25°C$, $\rho_0 = 6.9E\text{-}07$ kg/mm^3 and $\phi_0 = 0.08$

P	category	value	unit
λ_L	mechanical	11750	MPa
λ_{TR}	mechanical	44	MPa
μ_L	mechanical	650	MPa
μ_{TR}	mechanical	51	MPa
β^{λ}_{TR}	mechanical	1	-
β^{λ}_{L}	mechanical	1	-
$k^h_{1_L}$	mechanical	0	MPa
$k^h_{2_L}$	mechanical	10	MPa
k^h_{TR}	mechanical	2	MPa
$\sigma^Y_{c_L}$	mechanical	60	MPa
$\sigma^Y_{t_L}$	mechanical	110	MPa
$\sigma^Y_{c_T}$	mechanical	7	MPa
$\sigma^Y_{t_T}$	mechanical	7	MPa
$\sigma^Y_{c_R}$	mechanical	7	MPa
$\sigma^Y_{t_R}$	mechanical	7	MPa
$\sigma^Y_{c_{LR}}$	mechanical	7	MPa
$\sigma^Y_{t_{LR}}$	mechanical	7	MPa
$\sigma^Y_{c_{TR}}$	mechanical	7	MPa
$\sigma^Y_{t_{TR}}$	mechanical	7	MPa
$\sigma^Y_{c_{LT}}$	mechanical	7	MPa
$\sigma^Y_{t_{LT}}$	mechanical	7	MPa
α^L_t	thermo-mechanical	3.5E-06	1/K
α^R_t	thermo-mechanical	7.0E-06	1/K
α^T_t	thermo-mechanical	7.0E-06	1/K
$\rho_0 c$	thermal	1.7E+06	mm^2/(s^2 K)
k^L	thermal	0.16	W/(mm K)
k^R	thermal	0.17	W/(mm K)
k^T	thermal	0.17	W/(mm K)
α^L_m	hygro-mechanical	0.3	-
α^R_m	hygro-mechanical	1.3	-
α^T_m	hygro-mechanical	3.2	-
$c_{\varphi\vartheta}$	hygro-thermal	5.5E-08	1/(K s)
d^L	hygric	2.0E-09	kg/(s mm)
d^R	hygric	3.0E-10	kg/(s mm)
d^T	hygric	3.0E-10	kg/(s mm)
c_φ	hygric	1.0E-10	1/s

As shown in Fig. 7, the initial height (75 mm) of the mid-point of the top surface of the specimen is displaced by 30 mm after the heating process. Even after the springback, the computed position remains nearly constant. The prescribed and computed temperature change with respect to a reference temperature $\theta_0 = 298$ K for the mid-point of the top surface is shown in Fig. 8. After heating, an exponential-like drop of the top surface temperature at its mid-point is computed.

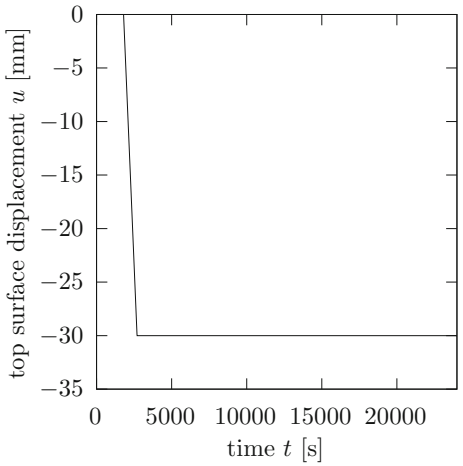

Fig. 7 Top surface mid-point displacement vs. time plot

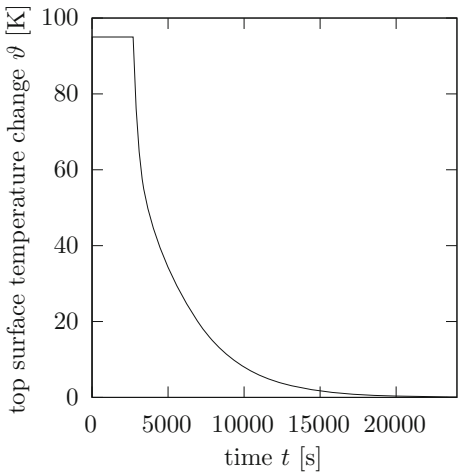

Fig. 8 Top surface mid-point temperature vs. time plot

In order to demonstrate the change of the density due to the compression set applied as well as the temperature distribution due to heating and cooling effects, Figures 10, 11 and 12 are given and cover the beginning, the middle and the end of the densification phase. The board represents the domain depicted in Fig. 13 before the springback and after cooling down. Figure 14 shows the change of the temperature and surface displacements right after the springback. The average density of the beech wood board is increased from 690 [kg/m^3] to approximately 1170 [kg/m^3] after a long cooling time.

The surface temperature distribution shown in Figs. 9 to 14 is not explicitly validated by experimental measurements, but will be implicitly validated in the following sections. The final density distribution shown in Fig. 14 leads to an averaged density of approx. 1170 [kg/m^3] which is nearly equal to the experimental data for 40% radially compressed beech wood of [56]. The next numerical result to be discussed is the amount of the instantaneous elastic springback $u_{sb} =$

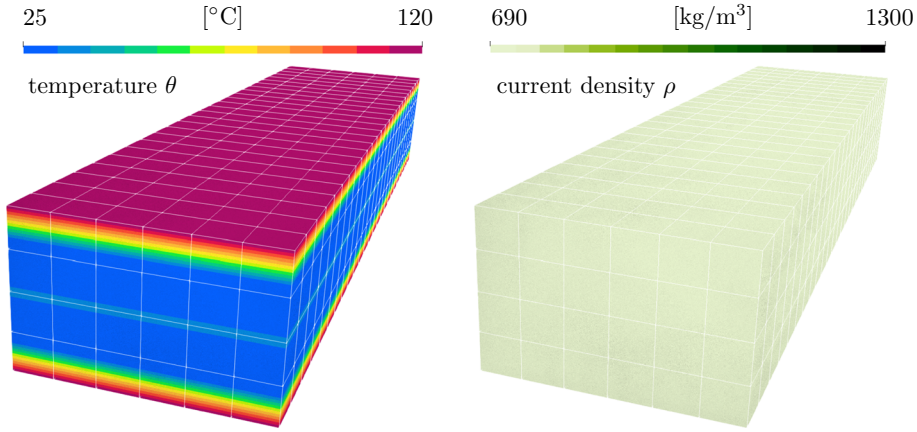

Fig. 9 Initial configuration of the mesh, temperature distribution (left) and density (right) at $t = 0$ s (beginning of heating)

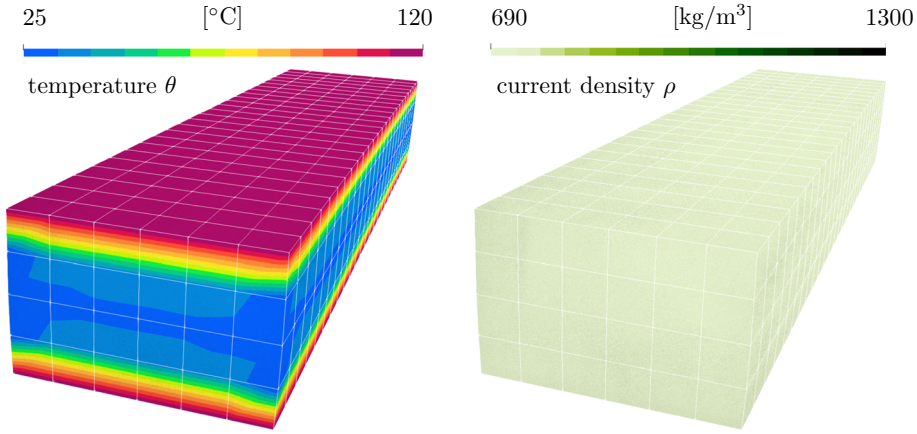

Fig. 10 Deformed configuration of the mesh, temperature distribution (left) and density (right) at $t = 1800$ s (after heating time)

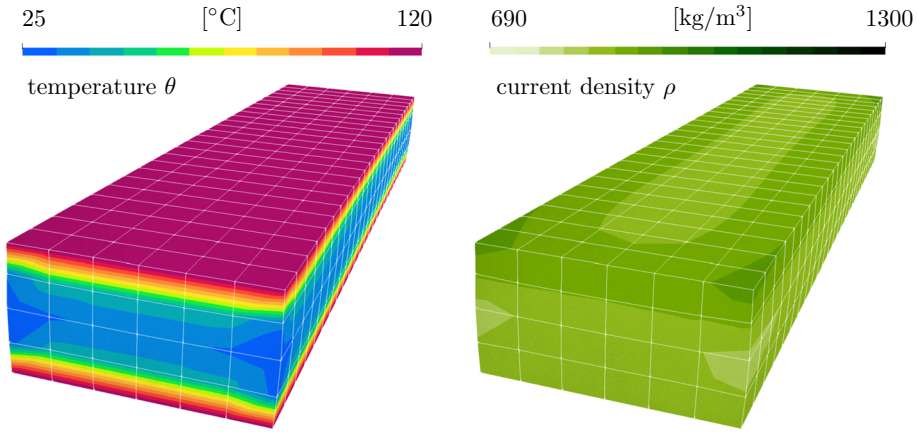

Fig. 11 Deformed configuration of the mesh, temperature distribution (left) and density (right) at $t = 2250$ s (during densification)

$u_{sb}(t_c)$ as a function of the cooling time t_c, see Fig. 15. The amount of the springback reduces by increasing cooling time, as can be seen in Fig. 15. Three simulations are carried out. At the first simulation, a cooling time of 1h is applied, in the second $t_c = 240$ min and in the third simulation, cooling time is adjusted to $t_c = 400$ min. This means, if a desired height of e.g. a densified board has to be achieved, a appropriate cooling time has to be considered, in order to bring the board into equilibrium between its internal energetic state and the environmental conditions.

During the heating, densification, holding and cooling simulations, the energetic state of the densified beech wood board is computed and, after the conducted process, the corresponding set of material parameter $\overline{P}$ is computed according to Eq. (77). The parameters, that do not enter the energetic functional, such as e.g. the yield stresses, are simply taken from the yield stress levels, published in [56]. The results in form of the predicted parameters of 40 % radially densified beech wood are given in Table 2. The omitted parameters, compared to Table 1, are assumed to be not sig-

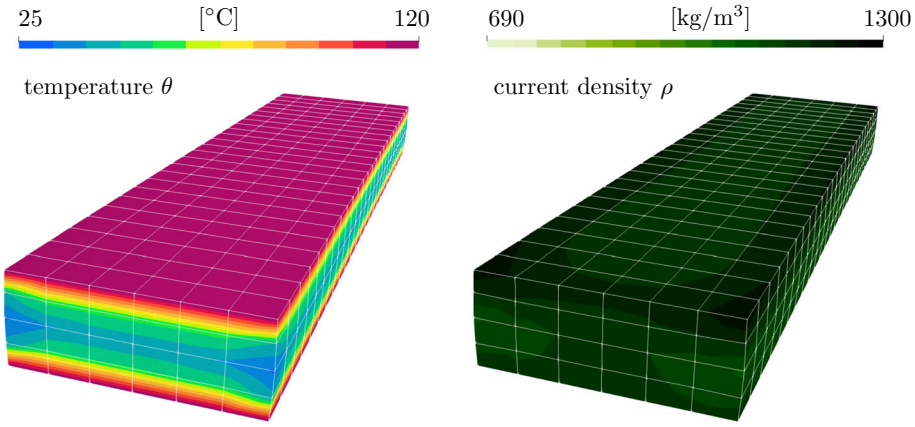

Fig. 12 Deformed configuration of the mesh, temperature distribution (left) and density (right) at $t = 2700$ s (after densification)

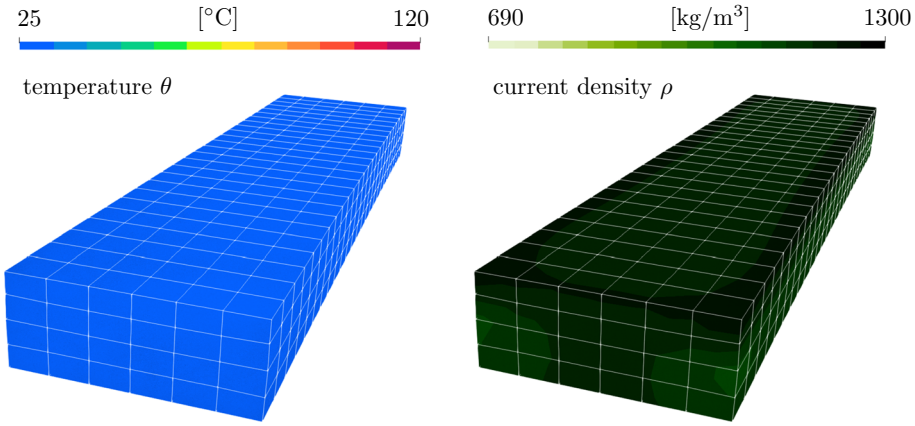

Fig. 13 Deformed configuration of the mesh, temperature distribution (left) and density (right) at $t = 24000$ s (before springback)

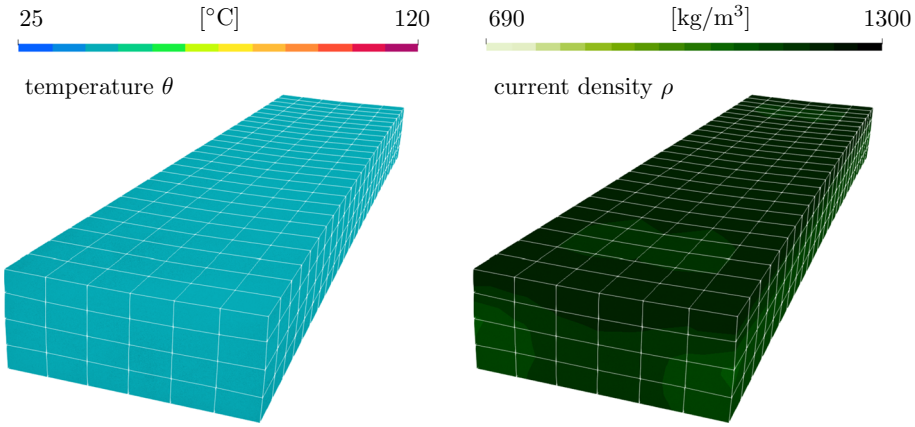

Fig. 14 Deformed configuration of the mesh, temperature distribution (left) and density (right) at $t = 24010$ s (after springback)

nificantly affected by a densification treatment. This means, that they are also valid for the reference values of $\theta_0 = 25°C$, $\rho_0 = 1.17\text{E-}06$ kg/mm^3 and $\phi_0 = 0.08$.

In order to validate the set of parameters in Table 2, the radial and tangential as well as longitudinal experiments in [56] are used, such that they are simulated and the results of the stress-strain plots are compared without any extra parameter fitting. Due to a limited number of experimental data on clear densified beech wood, such as stress strain graphs at different loads and specimens, the comprehensive modeling is only validated by the data given in [56]. This validation includes a specific set of production process parameters (e.g. heating and cooling times, temperatures, beech wood board geometries etc.). Nevertheless, there are no limitations of the proposed approach to predict compressed wood properties, e.g. of different wood species or different compression ratios.

The longitudinal tensile test specimen, made from densified beech wood, is exemplarily depicted in Fig. 16 as well as the Cauchy stress distribution at the final loading state of a strain value of 0.00412 [mm/mm]. The corresponding nominal stress strain plot is given in Fig. 17, where a good agreement between the simulation and the experiments is

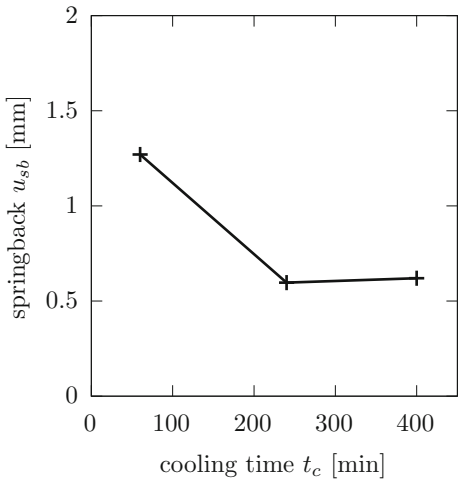

Fig. 15 Computed instantaneous springback as function of cooling time for an initial height of 75 mm and a radial compression set of 40 %

Table 2 Densified model parameter set $\overline{P}$ for radially compressed (40 %) beech wood at $\theta_0 = 25°C$, $\rho_0 = 1.17E\text{-}06$ kg/mm^3 and $\phi_0 = 0.08$

$\overline{P}$	category	value	unit	source
λ_L	mechanical	19925.27	MPa	Eq. (77)
λ_{TR}	mechanical	155.54	MPa	Eq. (77)
μ_L	mechanical	1108.11	MPa	Eq. (77)
μ_{TR}	mechanical	274.62	MPa	Eq. (77)
β^{λ}_{TR}	mechanical	0.41	-	Eq. (77)
β^{λ}_{L}	mechanical	0.33	-	Eq. (77)
$\sigma^{Y}_{c_L}$	mechanical	60	MPa	[56]
$\sigma^{Y}_{t_L}$	mechanical	120	MPa	[56]
$\sigma^{Y}_{c_T}$	mechanical	60	MPa	[56]
$\sigma^{Y}_{t_T}$	mechanical	40	MPa	[56]
$\sigma^{Y}_{c_R}$	mechanical	60	MPa	[56]
$\sigma^{Y}_{t_R}$	mechanical	40	MPa	[56]
$\sigma^{Y}_{c_{LR}}$	mechanical	7	MPa	[20,21]
$\sigma^{Y}_{t_{LR}}$	mechanical	7	MPa	[20,21]
$\sigma^{Y}_{c_{TR}}$	mechanical	7	MPa	[20,21]
$\sigma^{Y}_{t_{TR}}$	mechanical	7	MPa	[20,21]
$\sigma^{Y}_{c_{LT}}$	mechanical	7	MPa	[20,21]
$\sigma^{Y}_{t_{LT}}$	mechanical	7	MPa	[20,21]

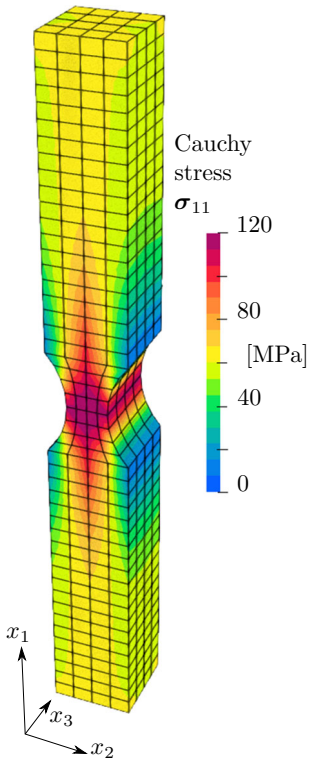

Fig. 16 Geometry of the tensile test specimen (taken from [55]) and computed tensile stress distribution for densified beech wood

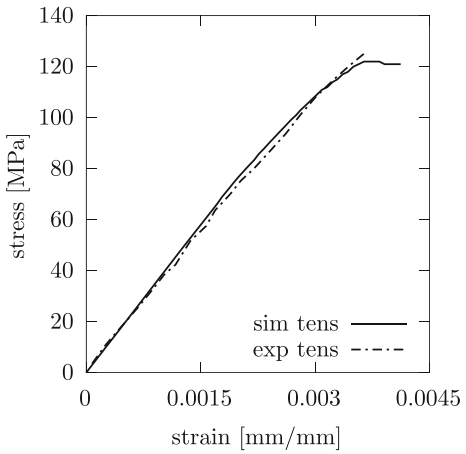

Fig. 17 Stress vs. strain plots for comparing experiments (exp) and simulations (sim) at 40 % densified beech wood in longitudinal tension (experiments taken from [56])

observable. Similarly, the stress strain plots for radial and tangential compression test simulations are in good agreement with the corresponding experimental measurements, see Fig. 18. The cube-shaped specimens are not depicted in extra figures but are described in [56].

From these numerical investigations, it can be concluded that the set of predicted parameters $\overline{P}$ in Table 2 describes the 40 % radially compressed beech wood in an appropriate manner. The validation is successful for radial and tangential compression as well as longitudinal tension. Therewith, the simulation results in Figs. 9 to 14 are implicitly validated too. Now, the finite element and finite surface element descriptions in Sect. 3 as well as the constitutive model in Sect. 4 in combination with the computation of effective parameters in Sect. 5.2 can be applied to simulations and analyzes of structures made from densified wood.

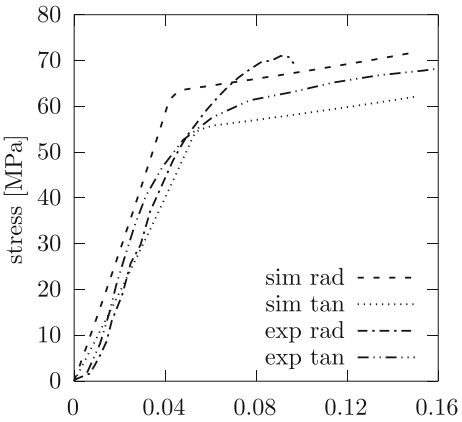

Fig. 18 Stress vs. strain plots for comparing experiments (exp) and simulations (sim) at 40 % densified beech wood in radial (rad) and tangential (tan) compression (experiments taken from [56])

6 Simulation of compression test at a molded wooden tube made from densified beech wood

Within the following section, a structural investigation of a molded wooden tube of densified beech wood is presented. The important fact to emphasize is the assemblage of the geometry from gamma-ray computed tomography (CT) data, available at [5]. Each 5 cm along the height (z-direction) of the tube, a CT-picture of the density $\overline{\rho}_0$ is taken, see [33] for a detailed description, and used for creating the FE-element mesh. The surface representation of the FE-mesh is shown in Fig. 19, where the CT data is applied each 10 cm along the height. The height of the tube is given by $h = 3.10$ m, while the thickness as well as the cross-sections of the tube differ along the height of the tube. Thus, no constant wall thickness or tube-diameter is given, but Fig. 19 contains a top and bottom view of the tube, to illustrate the geometrical imperfections. The material, densified beech wood, is parameterized by the set of model parameters, given in Table 2. Fig. 20 depicts the structural result of the compression test with respect to measured/computed force vs. displacement curves. The experiments show a slight shift with respect to the displacement axis, due to a lagged starting of the testing device and a delay in getting grip at the top and bottom of the tube, as discussed in [33], compared to the numerical simulation. But it can be noticed from Fig. 20 that the slope of both curves are nearly equal, i.e. the compressive elongation stiffness is well approximated by geometry and by the material parameters $\overline{P}$ from Table 2.

Figures 21 and 22 show a comparison of experiments and simulations of the surface strain data. The experiments are achieved by digital image correlation (DIC) and appropriate software, see [33]. The comparison is carried out such that at an equivalent load level, i.e. for a force value of 890 kN,

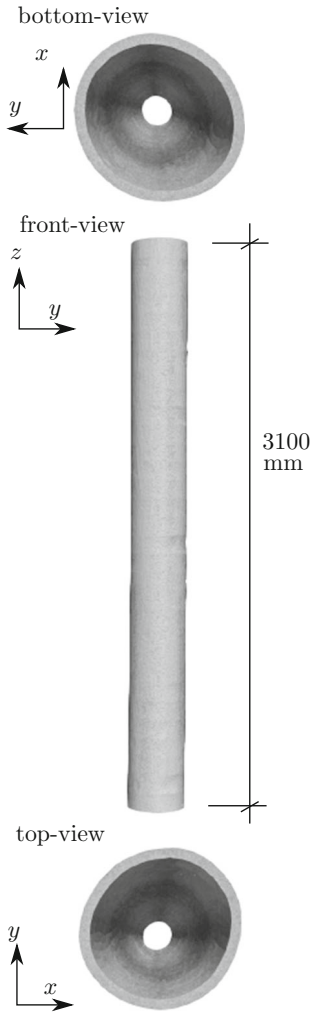

Fig. 19 Initial configuration of the mesh based on CT-data-set, taken from [5]

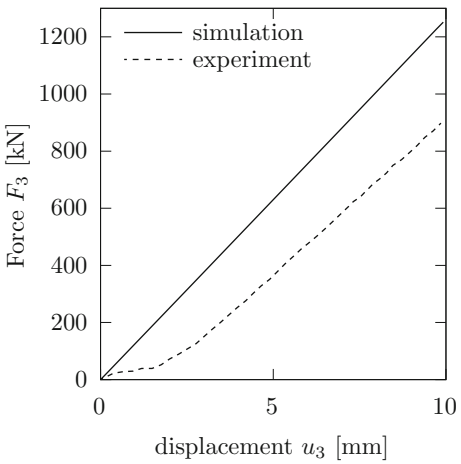

Fig. 20 Force vs. displacement plot comparing experiments and simulations for a molded wooden tube (experiments taken from [33])

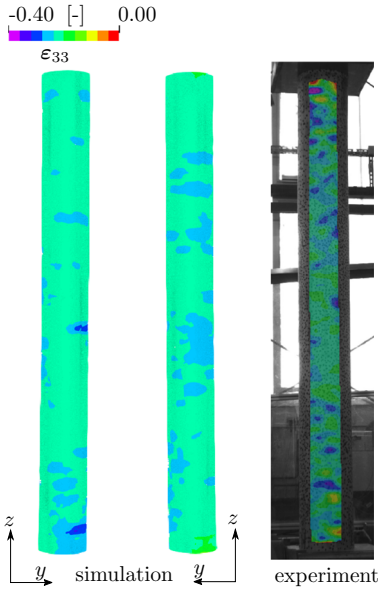

Fig. 21 Comparison of simulation and experiment (taken from [33]) for the longitudinal strain $\boldsymbol{\varepsilon}_{33}$

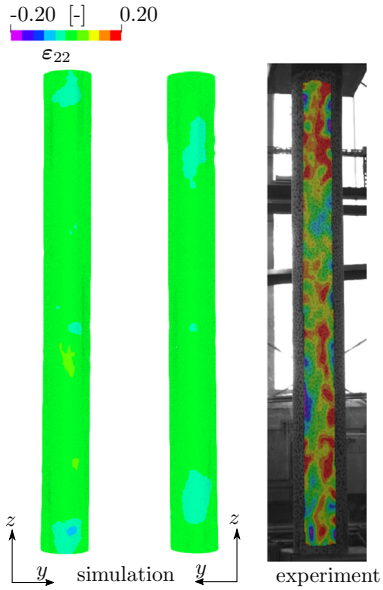

Fig. 22 Comparison of simulation and experiment (taken from [33]) for the transversal strain $\boldsymbol{\varepsilon}_{22}$

the related strains are compared. As can be seen in Fig. 21, a qualitatively good agreement between the both states of strain is observable. The strain distribution is not fully equal, since it is strongly depending on the geometry of the tube and the FE-mesh seems only to qualitatively match the real geometry every 10 cm. Figure 21 misses a qualitative good agreement between the simulated strain in y-direction and the measured strains. But the mean trend of slight positive averaged strains can be seen in both data sets. For sake of completeness, Figures 23 and 24 are given. The simulated Cauchy stresses cannot be compared to experiments. But especially in Fig. 24 it can be seen, that there is a correlation of the points with positive stresses and positive strains, measured by DIC. Thus, although the strain field in experiments and simulation do not fully match, at least, the stresses in y-direction have a weak correlation to the corresponding measured strain field.

7 Conclusion and outlook

Finally it can be stated that a comprehensive and general modeling of the densification process of wood, including the prediction of the instantaneous springback as a function of the cooling time, is introduced. This is achieved by a full consideration of the thermo-hygro-mechanical fundamentals of modeling wood at finite deformations as well as the related finite element formulations. The densification of wood intrinsically contains all required information, in order to predict the material characteristics and properties of the final and densified wooden structure. This phenomenon is successfully captured by an energetic approach to compute model parameters of densified wood. The methods and approaches are successfully validated for beech wood (*Fagus Sylvatica*). A simulation of the compression behavior of a tube like structure made from densified beech wood is shown.

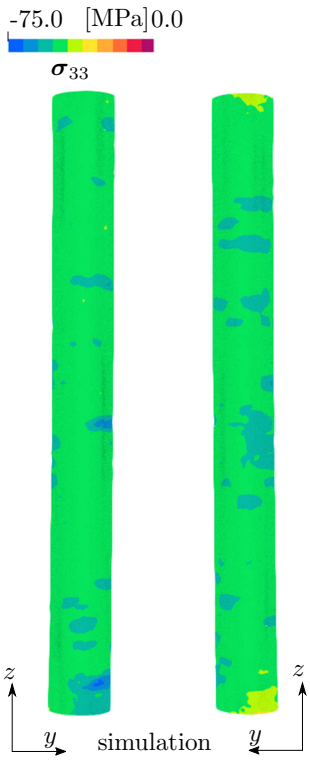

Fig. 23 Simulation results for the longitudinal Cauchy stresses $\boldsymbol{\sigma}_{33}$

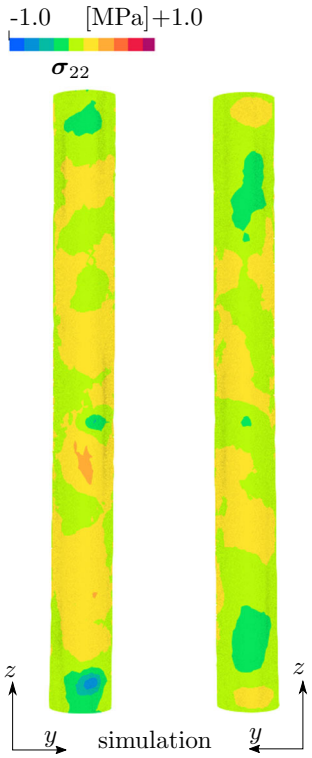

Fig. 24 Simulation results for the transversal Cauchy stresses σ_{22}

Having the ecological and environmental performance as well as the capabilities of wood in mind, the application of the current developments to other wood species, other process parameter sets etc. remains as open topic for further research with respect to simulation and experiments. Since the simulation of the compression of the wooden tube is showing globally a good agreement with the experimentally observed structural behavior but shows locally differences in comparison of simulation and experiments, a finer resolution of the tube components and geometry remains as open topic for further investigations. Additionally, numerical investigations of other structures made from densified wood remain as open research questions, in order to strengthen the usage and application of wooden products in general.

Acknowledgements This research is financially supported by the Deutsche Forschungsgemeinschaft (DFG) under contract KA 1163/22, which is gratefully acknowledged by the authors. Furthermore, the authors would like to thank the Chair of Timber Engineering and Construction Design at Technische Universität Dresden for fruitful discussions and helpful correspondence with respect to Sects. 5 and 6.

Funding Open Access funding enabled and organized by Projekt DEAL.

References

1. Abergel T, Dean B, Dulac J (2017) Towards a zero-emission, efficient, and resilient buildings and construction sector. Global Status Report 2017. United Nations Environment and International Energy Agency
2. Bathe KJ (1990) Finite-Elemente-Methoden. Springer, Berlin
3. Bayreuther C (2005) Mehrskalenmodelle in der Festkörpermechanik und Kopplung von Mehrgittermethoden mit Homogenisierungsverfahren. PhD thesis, Universität Stuttgart
4. Bazant ZP (1985) Constitutive equation of wood at variable humidity and temperature. Wood Sci Technol 19:159–177
5. Bieberle A, Engmann C, Hartig J, Haller P (2018) Analysis of moulded wood tube structure using gamma-ray computed tomography [Data set], https://doi.org/10.14278/rodare.55. *Rodare*
6. Carmeliet J, Guyer R, Derome D (2010) Moisture and mechanical hysteretic behavior of wood: a two-scale approach. In: Proceedings of the fourth European Conference on Computational Mechanics, Paris
7. Cave I (1978) Modelling moisture-related mechanical properties of wood. Part I Properties of the wood constituents. Wood Sci Technol 12:75–86
8. Cave I (1978) Modelling moisture-related mechanical properties of wood. Part II: Computation of properties of a model of wood and comparison with experimental data. Wood Sci Technol 12:127–139
9. Coleman BD, Gurtin ME (1967) Thermodynamics with Internal State Variables. J Chem Phys 47:597–613
10. Coleman BD, Noll W (1963) The thermodynamics of elastic materials with heat conduction and viscosity. Arch Ration Mech Anal 13:167–178
11. Curnier A, He Q-C, Zysset P (1995) Conewise linear elastic materials. J Elast 37:1–38
12. Davidzon MI (2012) Newton's law of cooling and its interpretation. Int J Heat Mass Transf 55:5397–5402
13. de Borst K, Jenkel C, Montero C, Colmars J, Gril J, Kaliske M, Eberhardsteiner J (2013) Mechanical characterization of wood: An integrative approach ranging from nanoscale to structure. Comput Struct 127:53–67
14. de Souza Neto EA, Perić D, Owen DRJ (2008) Computational Methods for Plasticity - Theory and Applications. Wiley, Chichester
15. Easterling KE, Harryson R, Gibson LJ, Ashby MF (1982) On the mechanics of balsa and other woods. Proc R Soc A 383:31–41
16. Eitelberger J, Hofstetter K (2010) Multiscale homogenization of wood transport properties: Diffusion coefficients for steady-state moisture transport. Wood Mat Sci Eng 5:97–103
17. Eitelberger J, Hofstetter K (2011) Prediction of transport properties of wood below the fiber saturation point - a multiscale homogenization approach and its experimental validation, Part II: Steady state moisture diffusion coefficient. Compos Sci Technol 71:145–151
18. Farruggia F, Perré P (2000) Microscopic tensile tests in the transverse plane of earlywood and latewood parts of spruce. Wood Sci Technol 34:65–82

19. Fleischhauer R, Bozic M, Kaliske M (2016) A novel approach to computational homogenization and its application to fully coupled two-scale thermomechanics. Comput Mech 58:769–796
20. Fleischhauer R, Hartig JU, Haller P, Kaliske M (2019) Moisture-dependent thermo-mechanical constitutive modeling of wood. Eng Comput 36:2–24
21. Fleischhauer R, Kaliske M (2018) Advances in Mechanics of Materials and Structural Analysis, chapter Hygro- and Thermo-Mechanical Modeling of Wood at Large Deformations: Application to Densification and Forming of Wooden Structures, pages 59–97. Springer, Cham
22. Fleischhauer R, Thomas T, Kato J, Terada K, Kaliske M (2020) Finite thermo-elastic decoupled two-scale analysis. Int J Numer Methods Eng 121:355–392
23. Frandsen HL (2005) Modelling of Moisture Transport in Wood – State of the Art and Analytic Discussion. Report, Aalborg University
24. Frandsen HL, Damkilde L, Svensson S (2007) A revised multi-Fickian moisture transport model to describe non-Fickian effects in wood. Holzforschung 61:563–572
25. Frandsen HL, Svensson S (2007) Implementation of sorption hysteresis in multi-fickian moisture transport. Holzforschung 61:693–701
26. Garab J, Keunecke D, Hering S, Szalai J, Niemz P (2010) Measurement of standard and off-axis elastic moduli and Poisson's ratios of spruce and yew wood in transverse plane. Wood Science and Technology 44:451–464
27. Gibson LJ, Ashby MF (2001) In: Cellular Solids - Structure and Properties, Chapter: Wood. Cambridge University Press, Cambridge
28. Goodman JR, Bodig J (1970) Orthotropic elastic properties of wood. J Struct Div - Proc Am Soc Civ Eng 96:2301–2319
29. Green A, Naghdi P (1971) Some remarks on elastic-plastic deformation at finite strain. Int J Eng Sci 9:1219–1229
30. Gustavsson L, Sathre R (2011) Energy and CO_2 analysis of wood substitution in construction. Clim Change 105:129–153
31. Hammoum F, Audebert P (1999) Modeling and simulation of (visco)-plastic behavior of wood under moisture change. Mech Res Commun 26:203–208
32. Hanhijärvi A, Mackenzie-Helnwein P (2003) Computational Analysis of Quality Reduction during Drying of Lumber due to Irrecoverable Deformation. I: Orthotropic Viscoelastic-Mechanosorptive-Plastic Material Model for the Transverse Plane of Wood. J Eng Mech 129:996–1005
33. Hartig JU, Bieberle A, Engmann C, Haller P (2021) Voxel-based finite element modelling of wood elements based on spatial density and geometry data using computed tomography. Holzforschung 75:742–753
34. Hartig JU, Wehsener J, Haller P (2016) Experimental and theoretical investigations on moulded wooden tubes made of beech (*Fagus sylvatica* L.). Constr Build Mater 126:527–536
35. Hassani MM, Wittel FK, Hering S, Herrmann HJ (2015) Rheological model for wood. Comput Methods Appl Mech Eng 283:1032–1060
36. Hauksson J, Bergqvist G, Bergsten U, Sjöström M, Edlund U (2001) Prediction of basic wood properties for norway spruce. intergretation of near infrared sprectroscopy data using partial least squares regression. Wood Sci Technol 35:475–485
37. Helnwein P, Eberhardsteiner J, Mang HA (2002) Modeling of biaxially stressed wood under planestress conditions as an orthotropic multi-surface elasto-plastic material. In: Proceedings of the Fifth World Congress on Computational Mechanics, Wien
38. Hering S, Keunecke D, Niemz P (2011) Moisture-dependent orthotropic elasticity of beech wood. Wood Sci Technol 46:927–938
39. Hering S, Saft S, Resch E, Niemz P, Kaliske M (2012) Characterisation of moisture-dependent plasticity of beech wood and its application to a multi-surface plasticity model. Holzforschung 66:373–380
40. Jenkel C, Kaliske M (2014) Finite element analysis of timber containing branches - an approach to model the grain course and the influence on the structural behaviour. Eng Struct 75:237–247
41. Jenkel C, Leichsenring F, Graf W, Kaliske M (2015) Stochastic modelling of uncertainty in timber engineering. Eng Struct 99:296–310
42. Kaliske M (2000) A formulation of elasticity and viscoelasticity for fibre reinforced material at small and finite strains. Comput Methods Appl Mech Eng 185:225–243
43. Kaliske M, Jenkel C, Saft S, Resch E (2010) Computational models for wooden structures. Computational Technol Rev 2:145–176
44. Kamke FA, Kutnar A (2011) Influence of stress level on compression deformation of wood in 170°C transient steam conditions. Wood Mat Sci Eng 6:105–111
45. Keunecke D, Hering S, Niemz P (2008) Three-dimensional elastic behaviour of common yew and norway spruce. Wood Sci Technol 42:633–647
46. Kleiber M (1972) A New Newton's Law of Cooling? Science 178:1283–1285
47. Kutnar A, Sandberg D, Haller P (2015) Compressed and moulded wood from processing to products. Holzforschung 69:885–897
48. Lee EH (1969) Elastic-Plastic Deformation at Finite Strains. ASME Journal of Applied Mechanics 36:1–6
49. Lubarda VA (2004) Constitutive theories based on the multiplicative decomposition of deformation gradient: Thermoelasticity, elastoplasticity, and biomechanics. Appl Mech Rev 57:95–108
50. Mahapatra K, Gustavsson L (2008) Multi-storey timber buildings: breaking industry path dependency. Build Res Inf 36:638–648
51. Marsden JE, Hughes TJR (1983) Mathematical Foundations of Elasticity. Dover Publications, New York
52. Miehe C (1988) Zur Numerischen Behandlung thermomechanischer Prozesse. PhD thesis, Universität Hannover
53. Miehe C (2003) Computational micro-to-macro transitions for discretized micro-structures of heterogeneous materials at finite strains based on the minimization of averaged incremental energy. Comput Methods Appl Mech Eng 192:559–591
54. Miehe C, Apel N, Lambrecht M (2002) Anisotropic additive plasticity in the logarithmic strain space: modular kinematic formulation and implementation based on incremental minimization principles for standard materials. Comput Methods Appl Mech Eng 191:5383–5425
55. Namari S (2022) Detailed informations on the specimen's geometries and experimental testing results. Personal correspondance
56. Namari S, Drosky L, Pudlitz B, Haller ASP, Bradley D, Mehra S, O'Ceallaigh C, Harte AM, El-Houjeyri I, Oudjene M, Guan Z (2021) Mechanical properties of compressed wood. Constr Build Mater 301:124269
57. Navi P, Sandberg D (2012) Thermo-Hydro-Mechanical Processing of Wood. Taylor and Francis Group, LLC, Lausanne
58. Niemz P (1993) Physik des Holzes und der Holzwerkstoffe. DRW-Verlag, Leinfelden-Echterdingen
59. Oudjene M, Khelifa M (2009) Elasto-plastic constitutive law for wood behaviour under compressive loadings. Constr Build Mater 23:3359–3366
60. Oudjene M, Khelifa M (2009) Finite element modelling of wooden structures at large deformations and brittle failure prediction. Mater Des 30:4081–4087
61. Reichel S, Kaliske M (2015) Hygro-mechanically coupled modelling of creep in wooden structures, part I: Mechanics. Int J Solids Struct 77:28–44

62. Reichel S, Kaliske M (2015) Hygro-mechanically coupled modelling of creep in wooden structures, part II: Influence of moisture content. Int J Solids Struct 77:45–64
63. Saft S, Kaliske M (2011) Numerical simulation of the ductile failure of mechanically and moisture loaded wooden structures. Comput Struct 89:2460–2470
64. Saft S, Kaliske M (2013) A hybrid interface-element for the simulation of moisture-induced cracks in wood. Eng Fract Mech 102:32–50
65. Sandberg D, Haller P, Navi P (2013) Thermo-hydro and thermo-hydro-mechanical wood processing: An opportunity for future environmentally friendly wood products. Wood Mat Sci Eng 8:64–88
66. Simo JC, Hughes TJR (1998) Computational Inelasticity. Springer, New York
67. Simo JC, Kennedy JG, Govindjee S (1988) Non-smooth multisurface plasticity and viscoplasticity. Loading/unloading conditions and numerical algorithms. Int J Numer Meth Eng 26:2161–2185
68. Tabiei A, Wu J (2000) Three-dimensional nonlinear orthotropic finite element material model for wood. Composite Structures
69. Temizer I, Wriggers P (2011) Homogenization in finite thermoelasticity. J Mech Phys Solids 59:344–372
70. Werner F, Richter K (2007) Wooden building products in comparative LCA. The Intern J Life Cycle Assess 12:470–479
71. Zhu Z, Kaliske M (2010) Numerical simulation of coupled heat and mass transfer in wood dried at high temperature. Heat Mass Transf 47:351-358
72. Zhu Z, Kaliske M (2011) Modeling of coupled heat, moisture transfer and mechanical deformations of wood during drying process. Eng Comput 28:802–827
73. Zienkiewicz OC, Taylor RL, Zhu JZ (2005) The Finite Element Method: Its Basis and Fundamentals, 6th edn. Elsevier Butterworth-Heinemann, Oxford